

# Tracing the Dark Matter Sheet in Phase-Space

Tom Abel<sup>\*</sup>, Oliver Hahn<sup>†</sup> & Ralf Kaehler<sup>‡</sup><sup>1</sup>

<sup>1</sup>*Kavli Institute for Particle Astrophysics and Cosmology, Stanford University,  
SLAC National Accelerator Laboratory, Menlo Park, CA 94025*

MNRAS submitted

## ABSTRACT

The primordial dark matter velocity dispersion is small compared to the velocities it attains during structure formation. Its initial density distribution is close to uniform and it occupies an initial sheet in phase-space that is single valued in velocity space. Because of gravitational forces this three dimensional manifold evolves in phase-space without ever tearing, conserving phase-space volume and preserving the connectivity of nearby points. N-body simulations already follow the motion of this sheet in phase-space. This fact can be used to extract full fine-grained phase-space structure information from existing cosmological N-body simulations. Particles are considered as the vertices of an unstructured three dimensional mesh moving in six dimensional phase-space. On this mesh, mass density and momentum are uniquely defined. We show how to obtain the space density of the fluid, detect caustics, and count the number of streams as well as their individual contributions to any point in configuration-space. We calculate the bulk velocity, local velocity dispersions, and densities from the sheet – all without averaging over control volumes. This gives a wealth of new information about dark matter fluid flow which had previously been thought of as inaccessible to N-body simulations. We outline how this mapping may be used to create new accurate collisionless fluid simulation codes that may be able to overcome the sparse sampling and unphysical two-body effects that plague current N-body techniques.

**Key words:** cosmology: theory, dark matter, large-scale structure of Universe – galaxies: formation – methods: numerical

## 1 MOTIVATION

For the past 40 years, N-body simulations have allowed to numerically study the evolution of the distribution of matter in the expanding Universe (Peebles 1971; Bertschinger 1998; Springel et al. 2005, cf.). A significant number of simulation codes have been developed for this purpose (e.g. Efsthathiou et al. 1985; Couchman 1991; Bryan & Norman 1997; Stadel 2001; Springel et al. 2001; Teyssier 2002; Wadsley et al. 2004, to name just a few). All such approaches to structure formation model the collisionless fluid of dark matter by a set of massive particles (typically of equal mass) and differ in how the gravitational forces are calculated at the positions of the particles. The forces are applied to update the velocities which in turn are used to update the positions. The system is then evolved forward in time. From such simulations much has been learned about the formation and evolution of cosmological structures and they have become a standard tool in physical cosmology. While three dimensional calculations have difficulty in sampling the six dimensional phase-space well (see e.g. Buchert & Bartelmann 1991) they have found

a very large range of applications and have driven much of the progress that has been made in the past decades of understanding structure formation. In quite a range of these applications the space density of the dark matter fluid is required and in many others the phase-space density is of great importance.

Some open questions that require detailed information about the dark matter density and its velocity distribution are related to dark matter detection. For the indirect detection techniques the predictions of dark matter annihilations luminosity on the density of the dark matter streams and the distribution and the relative velocities of the particles. Assuming well mixed phase-space and assuming a shape of the velocity distribution function this annihilation rate would scale with the square of the space density,  $\rho$ . In current, work these estimates are typically carried out by fitting spherical profiles to the main dark matter halo and its subhaloes and then assign annihilation luminosities by scaling the square of the smoothed halo and subhalo profiles appropriately. This smooths the dark matter fluid sufficiently to avoid noisy estimates of the annihilation signal (Diemand et al. 2008; Springel et al. 2008). However, in general the annihilation rates depend on the relative velocity of the dark matter particles interacting. Here one can distinguish between dark matter annihilation within individual streams of dark matter as well the contribution from

<sup>\*</sup> Email: tabel@stanford.edu

<sup>†</sup> Email: ohahn@stanford.edu

<sup>‡</sup> Email: kaehler@slac.stanford.edu

stream-stream interactions which differ strongly in the relative velocities (see e.g. Hogan 2001; Afshordi et al. 2009). This fine grained dark matter phase-space structure is equally important for considerations of dark matter direct detection experiments where one makes velocity cuts in the experimental analysis in order to reject certain backgrounds. The annular modulation of the relative velocity and the main dark matter streams in the solar neighborhood provided by the earth's motion around the sun allows one to potentially map the fine grained phase-space structure should the experiments be able to detect dark matter.

The best current approaches to probe the phase-space structures was surveyed by Maciejewski et al. (2009). These typically start with some tessellation of phase-space such as a Delaunay triangulation or a Voronoi tessellation (Bernardeau & van de Weygaert 1996), or cartesian trees (Sharma & Steinmetz 2006; Ascasibar 2010). The mass of the particles found within the cells give the local densities. When only space density is required, adaptive kernel smoothing is often employed. In fact, most images of dark matter simulations shown are projections of kernel smoothed particle distributions. Configuration space density estimators play a particularly important role when studying the topology and character of the cosmic web (e.g. Schaap & van de Weygaert 2000; Pelupessy et al. 2003; Aragón-Calvo et al. 2007; Colberg et al. 2008; Neyrinck 2008). However, in all cases, control volumes are defined such that they contain sufficient numbers of particles to reduce sampling noise. Unfortunately, this will average over large regions of configuration and phase-space and consequently effectively degrade the spatial resolution of the calculation.

In any case, there is ample motivation to study the distribution, evolution and current state of dark matter in the Universe further by observations as well as simulations. In this contribution we introduce a novel way to analyze  $N$ -body simulations. Our approach naturally arises from considering how the collisionless fluid of dark matter is expected to evolve in phase-space.

As is well known, (e.g. Shandarin & Zeldovich 1989), at early enough times, i.e. before shell crossing, the motion of the dark matter fluid is described by the Zel'dovich approximation (Zel'dovich 1970) as a potential flow

$$\mathbf{x}_t = \mathbf{q} + g_t \nabla \phi(\mathbf{q}), \quad (1)$$

$$\mathbf{v}_t = \dot{g}_t \nabla \phi(\mathbf{q}). \quad (2)$$

Here  $\phi$  is a potential field that is proportional to the initial gravitational potential field of perturbations,  $\mathbf{q}$  are the initial particle positions and  $g(t)$  is the growth factor of linear perturbations. At early times, i.e. for  $t \rightarrow 0$ , also  $g \rightarrow 0$ . These particles occupy a three dimensional submanifold  $S$  of the entire six dimensional phase-space with the time-dependent mapping:

$$\mathbf{q} \mapsto (\mathbf{q} + g_t \nabla \phi(\mathbf{q}), \dot{g}_t \nabla \phi(\mathbf{q})), \quad (3)$$

where for  $t \rightarrow 0$

$$\mathbf{q} \mapsto (\mathbf{q}, \dot{g}_0 \nabla \phi(\mathbf{q})), \quad (4)$$

the three-dimensional structure can be easily seen. This map is bijective until shell crossing occurs, i.e. when more than one stream of dark matter exists at one spatial location. We will refer to this three dimensional submanifold as the dark matter sheet (even when discussing it in one or two spatial dimensions). The volume of the sheet continues to grow as structure forms and evolves (Shandarin & Zeldovich 1989; Vogelsberger et al. 2008).

At the same time, current  $N$ -body simulations of structure formation do already follow individual dark matter particles through phase-space (e.g. Bertschinger 1998). The  $N$ -body technique thus corresponds to sampling the sheet at a finite number of points  $\mathbf{q}$  with the entire mass concentrated at their positions.

Vogelsberger et al. (2008); White & Vogelsberger (2009); Vogelsberger & White (2011) developed a powerful approach to augment cosmological simulations to record more knowledge about the evolution of this dark matter sheet. They derive an equation of motion for the distortion tensor around every particle to linear order and then evolve it with every particle during the simulation. They refer to this as the geodesic deviation equation (GDE). This gives access to information about the evolution of the stream density along every particle trajectory and allows to track the number of caustics an infinitesimal fluid element surrounding a dark matter particle will go through. This technique goes a long way in obtaining more information about the fine grained phase-space structure in dark matter halos (Vogelsberger & White 2011).

More restricted calculations in this context have been carried out in fixed potentials (Stiff et al. 2001) or one dimensions for Newtonian gravity (Alard & Colombi 2005) and General Relativity (Rasio et al. 1989). Also in the context of stellar dynamics there is a large body of literature which explores details of the phase-space structure of stellar system. From a numerical point of view the work of Cuperman et al. (1971) is particularly remarkable. Some 40 years ago these authors realized that in one dimension one can follow the phase-space boundary of a collisionless fluid and they give a beautiful implementation and calculations treating the phase-space fluid as a continuum. Studying the connection of their formalism to the  $N$ -body technique is revealing and what follows here is in some ways the extension to three dimensions with the exception of our approach to velocity dimensions and the way the Poisson equation is solved.

We suggest that the three-dimensional manifold can be decomposed by a space-filling grid that connects a finite number of vertices  $\mathbf{q}$ . The simplest version is to decompose the volume into three dimensional simplices, i.e. tetrahedra, which have the nice topological property of being either convex or degenerate. For any choice of a regular lattice of vertices  $\mathbf{q}$ , such a tetrahedral decomposition can be achieved by a Delaunay triangulation. In contrast to the particle discretization, we can now think of the dark matter mass being spread out over the corresponding volume elements.

This mesh traces the dark matter sheet as it subsequently evolves in phase-space. The motion of the mesh vertices are evolved using the Vlasov-Poisson equation of motion leading to complex foldings of the submanifold (e.g. Arnold et al. 1982; Tremaine 1999). Any such folding is coincidental with a volume inversion of a simplex. This volume inversion occurs when the simplex topologically evolves through a degenerate state (where the tetrahedron is planar because one vertex moves through the plane defined by the remaining three) which is equivalent to the emergence of a caustic. Note how this corresponds exactly to the sign changes of the distortion tensors of Vogelsberger et al. (2008) (their eq. 24).

The motion of the vertices does not change the connectivity of the mesh so that at all times the simplex structure can be constructed from knowledge of the  $\mathbf{q}$ . For cosmological  $N$ -body simulations, there exists a unique mapping between a particle ID and  $\mathbf{q}$ , so that the phase-space structure of the

dark matter sheet can be reconstructed at all times. Projecting the sheet onto configuration space gives then a volume filling density field of the dark matter fluid that we propose to use as the density field that should be used to solve Poisson's equation in future solvers for collisionless fluids. Current  $N$ -body solvers do not evolve the vertices consistently with a density field construed in the proposed way.

As a first step towards this goal, we analyze the results of standard cosmological  $N$ -body simulations using this new definition of the dark matter sheet. The plan of the paper is as follows. First we will explain one and two dimensional analogues to introduce the relevant concepts. We then describe the details of our implementation before we apply the method to analyze cosmological large-scale structure as well as the phase-space properties of a single galaxy cluster halo.

## 2 EVOLUTION OF THREE-DIMENSIONAL SHEETS IN PHASE-SPACE

The distribution function  $f(\mathbf{x}, \mathbf{p})$  describes the density of a fluid in phase-space. It evolves via

$$\frac{\partial f}{\partial t} = -\frac{\mathbf{p}}{m} \cdot \nabla_{\mathbf{x}} f - \nabla_{\mathbf{x}} \phi \cdot \nabla_{\mathbf{p}} f, \quad (5)$$

where  $\phi$  is the gravitational potential and  $m$  is the dark matter particle mass. Fluid elements get stretched in coordinate space by advection  $\frac{\mathbf{p}}{m} \cdot \nabla_{\mathbf{x}} f$ , and in the momentum coordinates by the gravitational forces  $\nabla_{\mathbf{x}} \phi \cdot \nabla_{\mathbf{p}} f$ . Note that in a Lagrangian frame the first term on the right hand side is zero. Furthermore, the second term describes how the fluid is stretched in momentum space and does not affect the space density of the fluid parcel. This just states Liouville's theorem (Gibbs 1902) that the volume in phase-space is conserved. Hence, any fluid volume  $\Delta \mathbf{x} \Delta \mathbf{v}$  will remain constant. We are interested here in the space density of the fluid, the projection of  $f$  into coordinate space. i.e. the integral  $\rho(\mathbf{x}) = \int f(\mathbf{x}, \mathbf{v}) d^3 v$ . The contribution to the space density of any stream of dark matter is only affected by the volume it occupies in the space coordinates, i.e.  $\Delta \mathbf{x}$ . Consequently, all that is necessary to follow the evolution of the dark matter density is to follow the Lagrangian evolution of fluid elements. The mass inside a volume element is conserved and its contribution to the space density of dark matter is described by the volume it occupies. Conversely, for a given WIMP model one knows the initial velocity dispersion at any point in space (e.g. Hogan 2001; Vogelsberger et al. 2008). Therefore, if one knows the spatial part of the phase-space density one has information about the density in velocity space. For a given shape of the initial distribution function in the velocity directions (e.g. a Maxwellian) one has a reliable measure of the intrinsic velocity density at all times.

It is instructive to first describe a straightforward and well known one-dimensional case from which a number of lessons can be learned which apply equally well in higher dimensions.

### 2.1 The Zel'dovich pancake

The phase-space diagram and the evolved density in a Zel'dovich plane wave collapse is shown in Figure 1. The initial sheet at very early times would be coincident with the  $x$ -axis as the initial velocity perturbation is small and the initial state models a nearly homogeneous Universe. Sampling this initial state with particles of equal mass gives one a grid of uniformly placed particles. Their configuration space volume

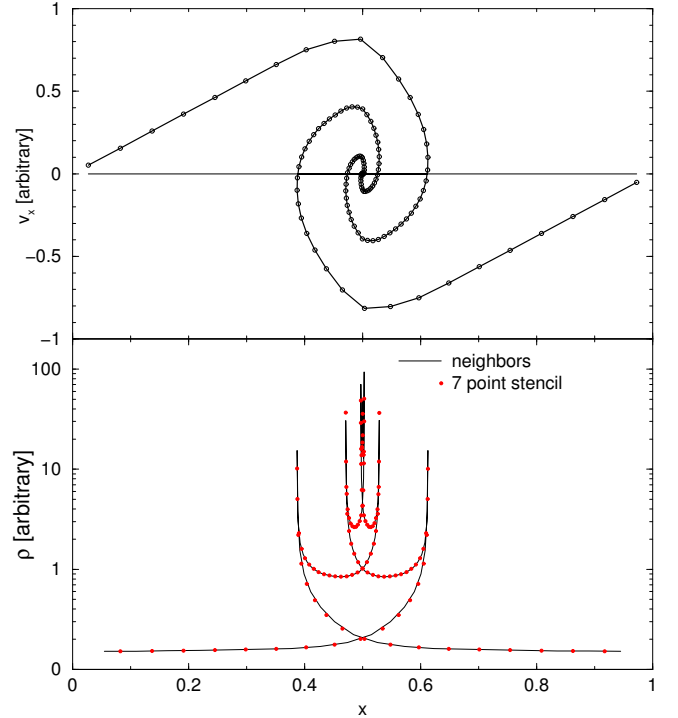


**Figure 1.** The one-dimensional plane wave collapse of Zel'dovich (Zel'dovich 1970; Binney 2004). The top panel gives the phase-space diagram showing the velocities of the particles at their locations. The bottom panel gives the density of the dark matter inside the stream, one computed with a seven point stencil (red squares), and the other computed from the volume between two neighboring points (solid line). Knowing the spatial volume between particles along one stream is sufficient to obtain accurate density estimates at and between the points.

is now directly related to their distance in the  $x$ -direction. Figure 1 shows the results of computing their local stream density from two approaches. In one, labelled “neighbour”, we take the  $V_i = x_{i+1} - x_i$  as the volume between particle  $i$  and  $i + 1$ . One full particle mass is distributed in this volume and the density at  $(x_i + x_{i+1})/2$  is given by  $\rho_{neigh} = m_p/|V|$ . The values shown as “squares” in the same figure are computed including information from points further along the stream,  $\rho_{7pt} = 6 m_p/|x_{i+3} - x_{i-3}|$ . It is defined at the particle position  $x_i$ . A number of observations can be made. Volumes defined in this way may be positive or negative depending on whether particles have the same or opposite ordering that they had initially. Volume elements may also become 0. The density involving more points along the stream gives rise to some smoothing and density extrema are clipped. The central high configuration space densities are reached for two reasons. The primordial stream densities along the sheet become larger and many streams overlap adding their densities. The number of streams in space is always an odd number at any location in space. Only at the caustics may one measure even numbers.

The particle locations trace the sheet in phase-space. Any unstructured space-filling grid that connects adjacent fluid elements may be used to trace the dark matter sheet as it evolves in phase-space. In fact, there is significant ambiguity here as illustrated in Figure 2. The two-dimensional analog shown there has as a simplex triangles. The smallest possible elements one may choose to follow would be the Delaunay triangulation of the points. However, these would give two resolution

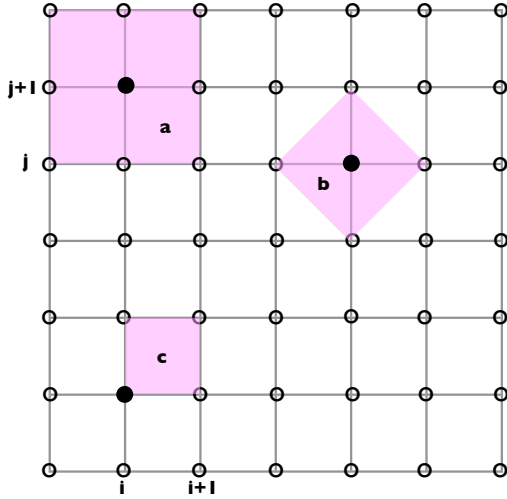


**Figure 2.** There are a number of possible cell elements one may consider as the unit cell that tessellates the three dimensional dark matter sheet which connects the particles of an  $N$ -body simulation.

elements per square initial cell. It would seem unreasonable that the mass of the fluid would be conserved exactly in each element, given that we only have information at the vertices. This could only be true if the mesh points were not distorted very much and the gradients of the flow, both in configuration and momentum space had length scales much larger than the sides of the triangle. However, case a) depicted in the figure would likely be a better choice as a fundamental resolution element as its eight nodes on the surface would be able to more accurately describe the deformations caused by the flow pattern. The mass inside that boundary would be conserved to a better degree than choices for a fundamental resolution element with smaller area. Note, however, that we still can use triangles to calculate the volume (area in 2D) of the sheet.

After considering some preliminaries in one and two dimensions, let us proceed to the three-dimensional case.

## 2.2 An Unstructured Grid to trace the Dark Matter Sheet in phase-space

The simplex in three dimensions is the tetrahedron. We will use it to calculate volumes and tessellate our chosen fundamental volume element. This is exactly equivalent to choosing line elements in one and triangles in two dimensions as the elements which are summed in volume calculations. Figure 3 shows one of the choices we have employed to tessellate a cubical fundamental cell. The figure also gives the numbering of vertices and of the six tetrahedra which make up the cell. The connectivity of vertices is chosen such that in a regular uniform grid all tetrahedron volumes are positive. For much of the calculation we keep the sign, because as we will see it can be a useful diagnostic of the flow. If we shift a tetrahedron such that one vertex coincides with the origin, the volume is simply given from the determinant or equivalently from a scalar and a cross product involving its other three vertices,  $V = \det[\mathbf{a}, \mathbf{b}, \mathbf{c}] / 6 = \mathbf{a} \cdot (\mathbf{b} \times \mathbf{c}) / 6$ . This implies that the volume can be negative if the tetrahedron has been turned inside out. As a choice of fundamental volume element we consider the 24 tetrahedra around each point which abut to a given vertex. Their volumes are thought of containing four times the mass

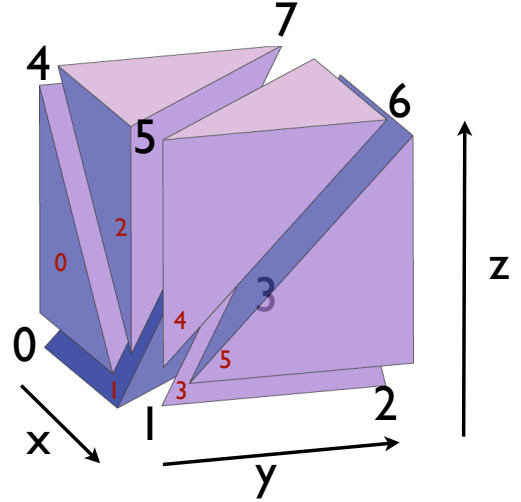


**Figure 3.** One of the possible tessellations of a cubical cells into tetrahedra. This choice gives 6 tetrahedra all of equal volume fraction. This particular choice has two of the cube corners being vertices for all tetrahedra and has the other corners be connected to two tetrahedra each.

of one particle. This effectively averages the density field on a kernel of the same size as four cubical volumes.

In a simple implementation, the vertices of the tessellation correspond to the particles of a standard  $N$ -body simulation. This implies that the vertices are moving in a Lagrangian way so that the spatial sampling is degrading over time in low-density regions and improving in high-density regions. One implication of the Lagrangian motion of the mesh vertices is that unresolved volume elements may not evolve according to the properties of the underlying flow. One particular such example is given in Figure 4 which illustrates that volume elements covering a divergent flow can evolve as if they were in a convergent flow if only the vertices are convergent. This behaviour implies that single volume elements, i.e. tetrahedra, of our space discretization are not to be trusted as perfect bags of fluid. In the example from Figure 4, the single tetrahedron suggests that shell-crossing occurred across a divergent flow which is unphysical – e.g. implying spurious links between haloes across unresolved void regions in cosmological context.

There are two possibilities to achieve a more robust density estimate: (1) The volume estimates of several tetrahedra are combined, so that density estimates are based on a larger region of the flow, or (2) local refinement of the volume elements is performed whenever e.g. axis ratios or curvature in phase-space suggest that the volume element might be ill-resolving the flow properties. The second option is certainly the more exciting possibility to achieve a density estimation method that is well consistent with flow properties. It requires however that the discretized dark matter sheet is refined while the  $N$ -body simulation is run, so that the newly inserted vertices are evolved with the flow. For this reason, we first focus on an evaluation of the averaging approach in this paper and consider refinement strategies in a future publication.

## 2.3 Implementation: Computing the stream properties

The choice of tetrahedra used for most of the plots in this paper were given with a slightly different tessellation than the one

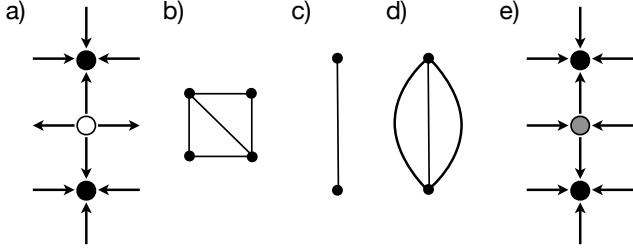


**Figure 4.** The need to resolve critical points of the flow: a) a halo-void-halo configuration that, when probed with a tetrahedral structure b), leads to a final state of the structure as given in c). The correct motion of the fluid element would have been as shown in d). Instead, the lack of resolution around critical points leads to a solution that would have been correct for the halo-filament-halo configuration shown in e). Hence a) and e) are indistinguishable when only looking at the vertex information of the fluid element b). The loss of spatial resolution can be circumvented by smoothing or by adaptive refinement of the volume elements.

shown in Figure 3. The connectivity list for the six tetrahedra specifically is [4, 0, 3, 1], [7, 4, 3, 1], [7, 5, 4, 1], [7, 2, 5, 1], [7, 3, 2, 1], [7, 6, 5, 2] where the unit cube vertices are labeled as in Figure 3. We define the fundamental volume element surrounding any vertex  $\mathbf{x}$  as the union of all the tetrahedra that share this vertex. The volume of the union is computed using the modulus of the volumes, i.e. inverted tetrahedra are not subtracted. Such a volume carries the mass of four particles which allows us to estimate the local density. This local average over adjacent tetrahedra we call the “primordial” stream density. It is a well defined quantity even after shell-crossing, it, however, is only defined for the vertices  $\mathbf{x}$  of the tessellation.

The next step in calculating a configuration space density estimate, as well as in evaluating other stream properties is an integration through velocity space. This is achieved by finding all intersections of tetrahedra with the point  $\mathbf{y}$  at which the density or other properties are to be determined. We refer to all these intersections which are not part of the primordial stream as the “secondary” streams.

At the heart of a fast algorithm is thus a way to speed up this search for point-tetrahedron-collisions. At first sight it requires  $6 * N^2$  searches given that we have six tetrahedra per particle and  $N$  particles. However, this can be radically improved using a chaining mesh that organizes tetrahedra contained in mesh cells or use tree structures which group tetrahedra into regions of space they occupy. One could use six trees, e.g., to organize bounding boxes containing tetrahedra which is advantageous as they are generally smaller than the circumsphere of tetrahedra which would require less storage. We, however, implemented two other versions. One with a chaining mesh and another that employs three bounding-box oct-trees offset from each other containing disjoint sets of tetrahedra so that tetrahedra cutting along tree node boundaries only do so typically for one of the trees. We then parallelized the search with OpenMP and arrived at a very practical tool to carry out the tessellation and measure the quantities we were interested in.

Since  $\mathbf{y}$  will typically lie inside a tetrahedron, we can now interpolate the primordial stream density defined at the vertices of this tetrahedron to  $\mathbf{y}$ . We use a one-over-distance-squared weighting (Shepard’s method) when we need to query information away from vertices. Thus, quantities such as the total configuration space density are then obtained by find-

number particles	$m_p/h^{-1}M_\odot$	$\epsilon/h^{-1}\text{kpc}$
$32^3$	$1.50 \times 10^{11}$	100
$64^3$	$1.87 \times 10^{10}$	50
$128^3$	$2.34 \times 10^9$	25
$256^3$	$2.92 \times 10^8$	10

**Table 1.** The specifics of the suite of  $N$ -body simulations used in this paper. All simulations are of a  $40 h^{-1}\text{Mpc}$  cosmological volume,  $m_p$  is the particle mass,  $\epsilon$  the force softening.

ing all tetrahedra that contain the point under consideration and summing over all of them. When evaluating velocities, we define the velocity field inside of a tetrahedron as the average over the velocities of the four particles that constitute its vertices.

To be more explicit let us emphasize that all that follows below is carried out purely from post-processing existing simulations. No line of code has to be changed in the readers favorite cosmology code. As long as it writes out the particle IDs at every snapshot of the simulation you can postprocess simulations you already have and measure, visualise and analyse it in new ways.

With these definitions and implementation details in hand we now proceed to applying the method for a number of  $N$ -body simulations of large scale structure formation.

### 3 APPLICATIONS

For our first applications we chose to test the method on simulations of the same physical scale differing only in numerical resolution.

#### 3.1 $N$ -body Simulations

We have carried out cosmological  $N$ -body simulations of a volume of  $40 h^{-1}\text{Mpc}$  length, run with the tree-PM code GADGET-2 (Springel 2005). The initial conditions for these single-mass-resolution simulations were generated with the MUSIC code (Hahn & Abel 2011) keeping large-scale phases identical with changing mass and spatial resolution. We assume a concordance  $\Lambda\text{CDM}$  cosmological model with density parameters  $\Omega_m = 0.276$ ,  $\Omega_\Lambda = 0.724$ , power spectrum normalization  $\sigma_8 = 0.811$ , Hubble constant  $H_0 = 100 h \text{ km s}^{-1} \text{ Mpc}^{-1}$  with  $h = 0.703$  and a spectral index  $n_s = 0.961$ . The particle numbers, masses and force softenings of these simulations are summarized in Table 1. Very clearly this box is much too small for careful statistical analysis of the cosmic web. However, we chose it here to give us the opportunity to study how our method converges at different mass resolution both in the collapsed objects as well as in the cosmic web. A number of the quantities we measure should hence not be understood as final numbers/answers. Similarly, the highest resolution simulation we discuss here takes very little computational resources. However, as we will see, it will suffice to demonstrate the advantages of the new approach.

#### 3.2 Large Scale Structure & Streams

Our method allows to separate physically distinct structures. The number of streams at a given location can only ever be



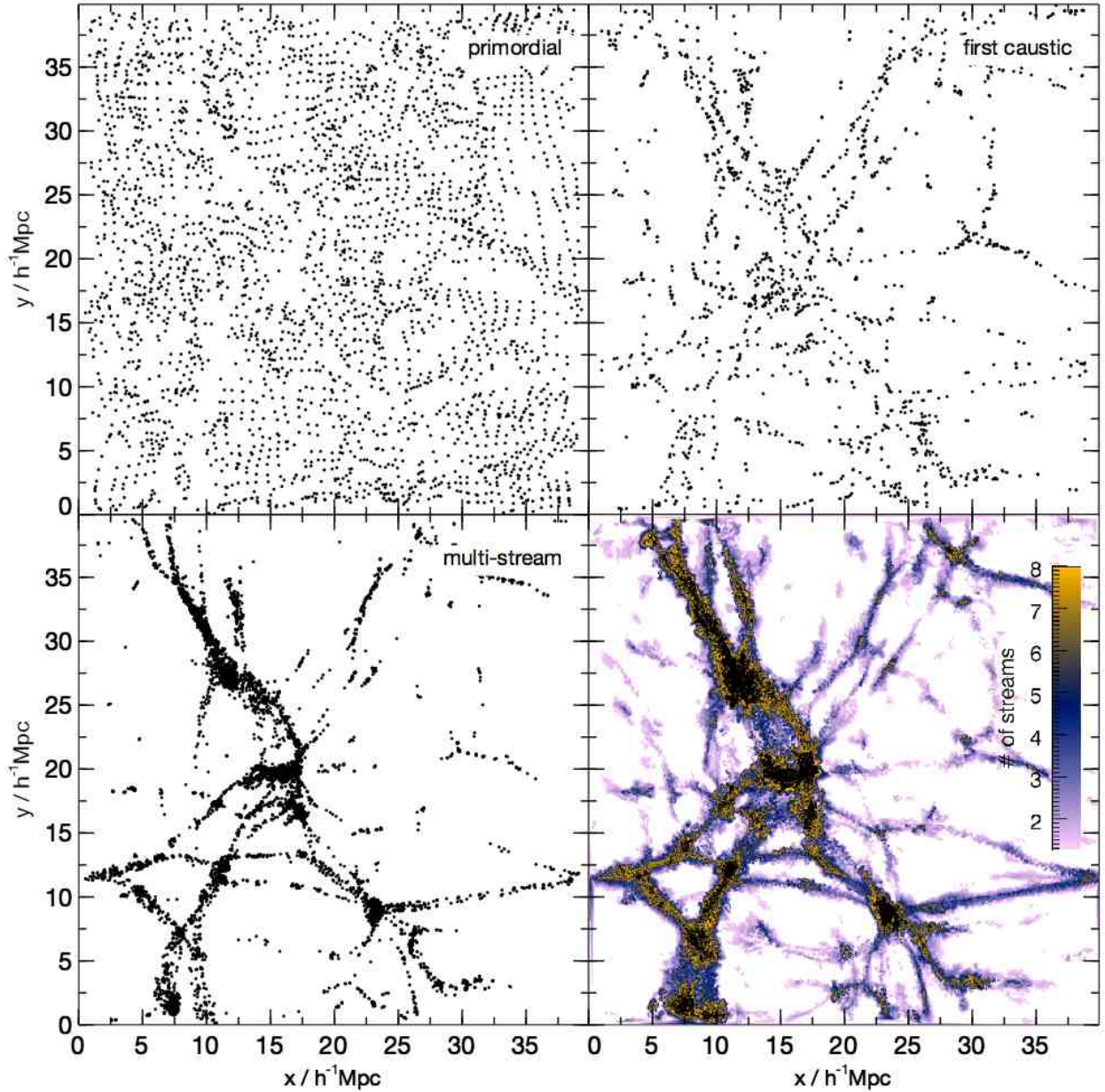


**Figure 5.** Particles with different numbers of streams in a slice  $0.5h^{-1}\text{Mpc}$  thick. Top left: particles whose primordial stream does not overlap with other parts of the sheet. Top right: particles which are on their first caustic, i.e. they measure a number of streams of two at their location. Bottom left: particles for which the number of streams is greater to or equal to three. Bottom right gives the average number of streams on an infinitesimally thin slice. Distinct physical components become clearly visible and separated.

an odd number as any fold will add two more streams to an existing one (e.g. Arnold et al. 1982; Shandarin & Zeldovich 1989). The notable exception is at the location of caustics where points may sit such as to only measure an odd number of additional streams. For the number of streams defined at the particle positions we can use this fact to select the structures that are constituting the first caustic. We illustrate the meaning of the local number of streams in Figure 5. The particles that record that they are part of only their primordial stream clearly define the voids at the mass scale that is resolved in the calculations. Particles that count two streams surround the sheets formed between voids. When they undergo their first caustic they have already crossed through the sheet and are turning around on the side opposite to from where they fell in from. The particles which measure three or more streams are

also shown and they trace the location of the collapsed objects well. We still consider all particles which count two streams or more as part of collapsed objects. This is the same decomposition that can be made in the GDE approach of Vogelsberger et al. (2008) as shown for the environment of Aquarius halos in Vera-Ciro et al. (2011) (their Figure B1) and Vogelsberger & White (2011) (their Figure 4).

We can see the distributions of the mass fractions as a function of the number of streams in Figure 6. We plot them for particles recording odd and even counts separately. One may have expected that the fraction of particles that are on caustics vs particles that have odd numbers of streams to decrease, as the caustics are better resolved for the high resolution runs. Instead, the offset between odd and even numbered mass fractions is approximately constant. This is just a feature

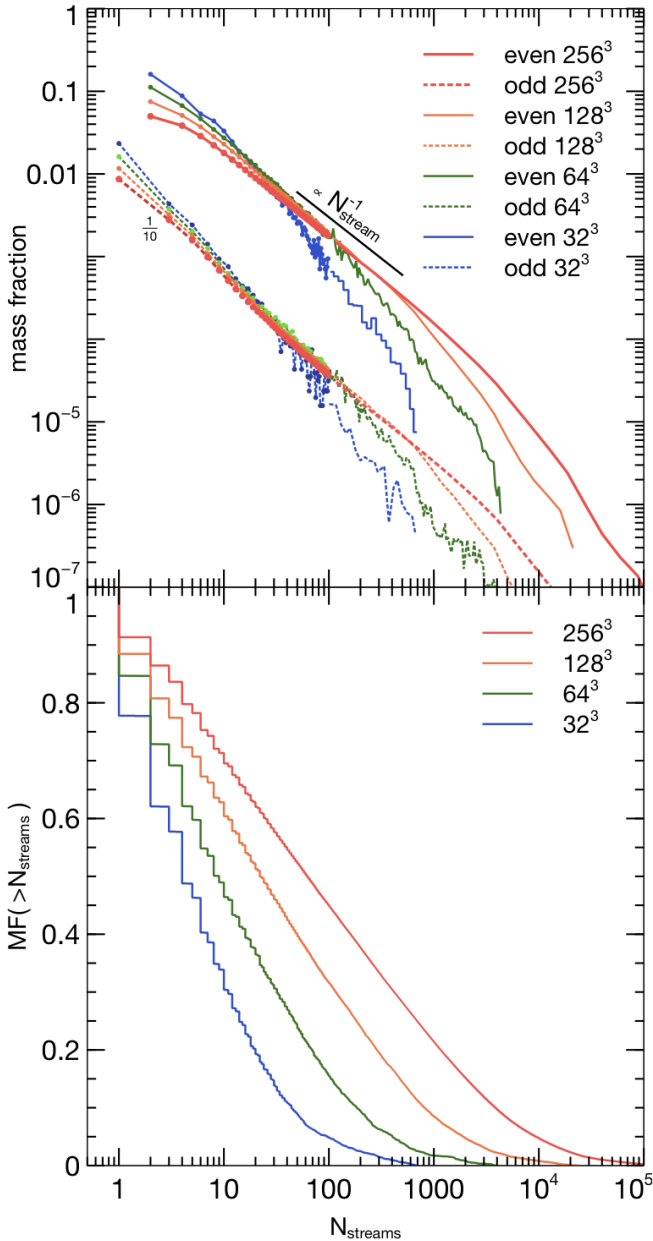


**Figure 6.** The mass fraction distribution in streams. Many more odd numbers of streams are found than even ones. We show them as separate lines with the odd ones displaced down by a factor of ten for clarity. They differ by a factor approximately 4 and that ratio does not depend much on the resolution of the underlying dark matter simulation. An asymptotic slope of  $\sim N_{\text{stream}}^{-1}$  develops for the higher resolutions for an intermediate number of streams. At low resolution steeper relations are inferred. For our most resolved simulations about 90 per cent of the mass is in collapsed structures. Some 50 per cent of the mass is in locations with 20 streams or more.

of cold dark matter simulations that with increasing resolution also more smaller objects can be resolved. This is illustrated directly in the bottom panel of that Figure. The cumulative distribution of mass above a given number of streams clearly does not converge. This just reflects that there are many small scale density fluctuations that collapse even earlier when the simulations can resolve them. It is quite plausible that the total fraction of collapsed mass will ultimately approach the very

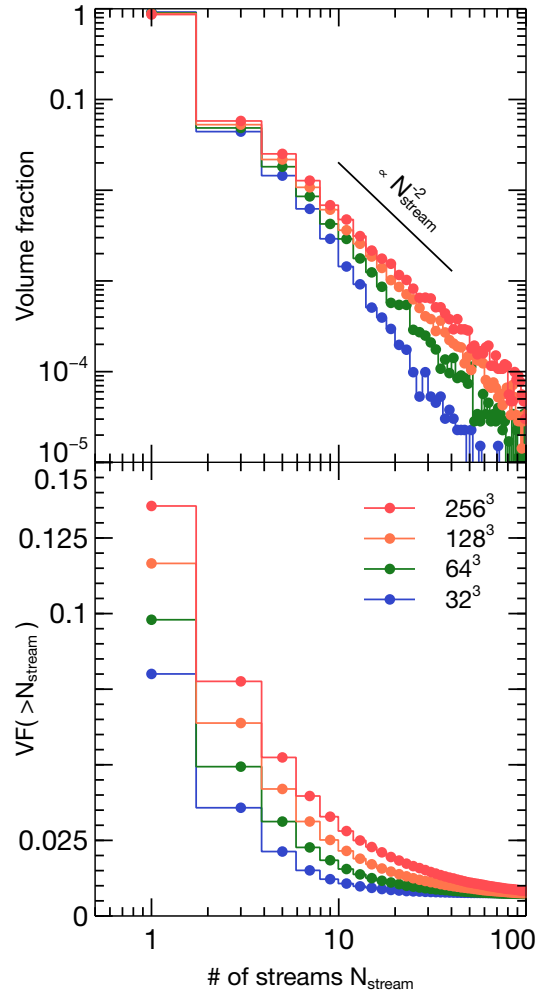


**Figure 7.** The volume fraction distribution in streams; a resolution study. For our most resolved simulations about 85% of the volume is in voids, around 7 (14) per cent is in collapsed structures ( $N_{\text{streams}}$  larger or equal to three) for the  $128^3$  ( $256^3$ ) run. The fraction of volume taken up by collapsed objects does not converge as expected.

high value of 99 per cent that has been estimated analytically by Shen et al. (2006) from the ellipsoidal collapse model.

For the volume averaged fraction as a function of streams and the corresponding cumulative distribution in Figure 7, we observe a similar lack of convergence. Smaller and smaller pancakes are resolved as the resolution increases making more and more volume have had shell crossing in the past.

It is clear from these results that questions about the shell-crossed mass and volume fractions in cold dark matter simulations are intimately tied to a scale. Only when introducing such a scale, e.g. through filtering of density perturbations or a constant force softening across resolutions, we could hope to obtain a meaningful measure of these quantities.

This is compatible with previous results on mass and volume fractions in the various parts of the cosmic web e.g. by Hahn et al. (2007) using a fixed scale, or by Aragón-Calvo et al. (2010) using adaptive filtering. In both cases the filtering scales are related to the non-linear scales today which is the relevant scale for much of galaxy formation.

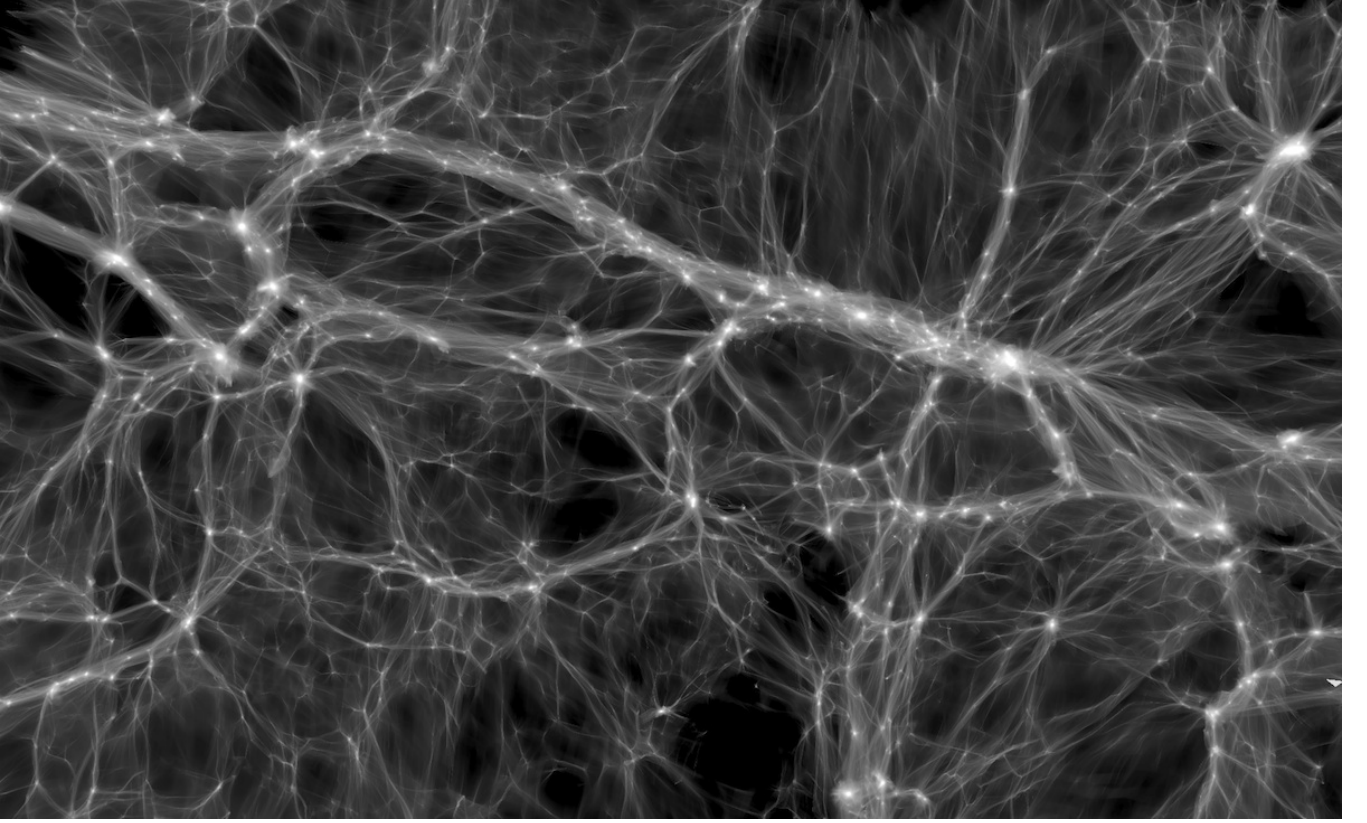


**Figure 8.** A rendering of the projected dark matter density in the  $256^3$  run using our density estimator and our custom GPU based renderer.

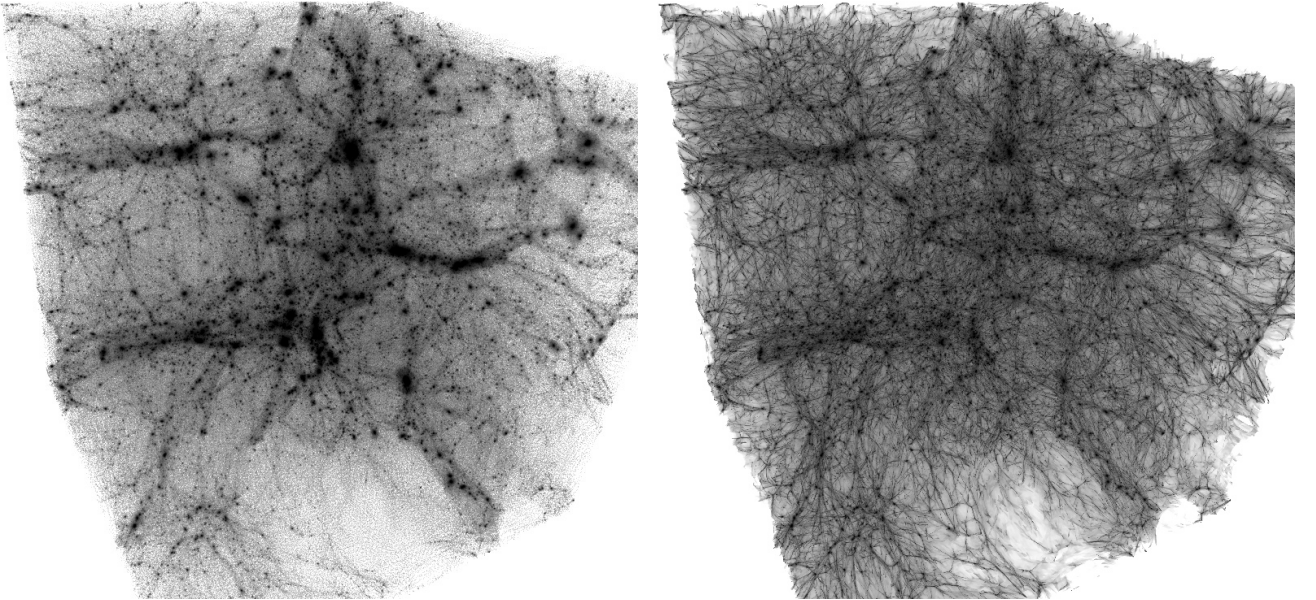


**Figure 9.** Comparison of the visual appearance of renderings of the dark matter density in the  $256^3$  run using our new density estimator as compared to adding pixel values that contain dark matter particles. While many of the well sampled regions are clearly apparent in both, the detailed structure of filaments, sheets and how they connect to voids becomes only apparent in our new approach shown on the right.



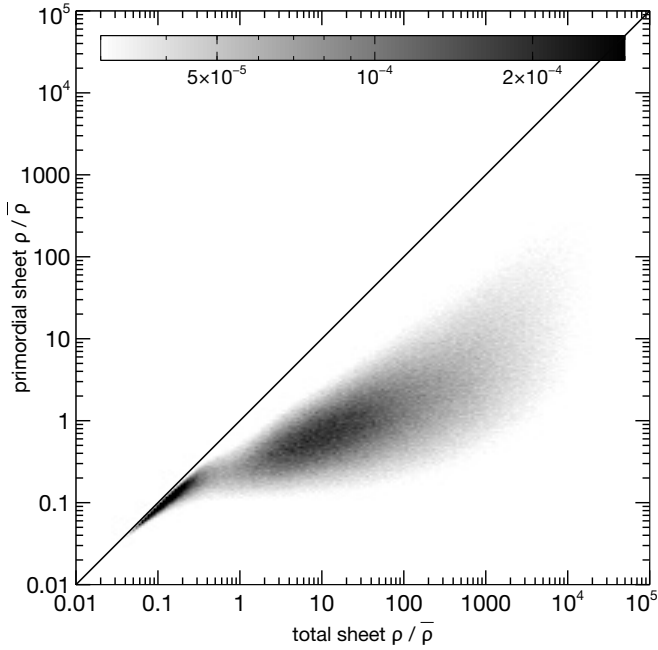


**Figure 10.** Two dimensional mass-weighted histogram comparing the density of the primordial dark matter sheet to the total sheet density in the  $128^3$  simulation. Much of the mass is contained at configuration space densities about ten times the mean. The primordial stream density also scatters very much but its median density is close to the average density of the Universe.

### 3.3 Visualization

The method presented here also is an ideal tool to visualize the data from current N-body simulations and thus to further help extracting physical insights from the calculations. Figure 8 gives an example that we have obtained with a custom-written OpenGL based renderer of the tetrahedral mesh. The primordial stream densities are averaged over abutting tetrahedra as described in the implementation section above. Then tetrahedra are splatted, taking advantage of the OpenGL primitives designed specifically for polygonal meshes. The length integral through the assumed uniform tetrahedron is found from evaluating the depths of front and back faces using their normals. This can then be integrated (accumulated on pixels) along all lines of sight.

We compare this to the visual impression one obtains by plotting individual points of a calculation vs. our new density definition in Figure 9. One can clearly see how filaments and sheets in and surrounding voids can be distinguished easily now. The visual impression is commensurate with the statistics we present next.

### 3.4 Dark Matter Densities

Figure 10 gives the relation of the density in the primordial stream to the total density evaluated at the locations of all the particles, i.e. a mass weighted histogram. At low densities these are identical as this material is traced by the original sheet and no folding has occurred. There is an enormous scatter at higher densities which we can quantify further. Figure 11 gives the mass-weighted density distribution for all the simulations we have analyzed. The top panel summarizes the individual contributions for the  $256^3$  simulation. The primordial stream density distribution peaks slightly below mean density

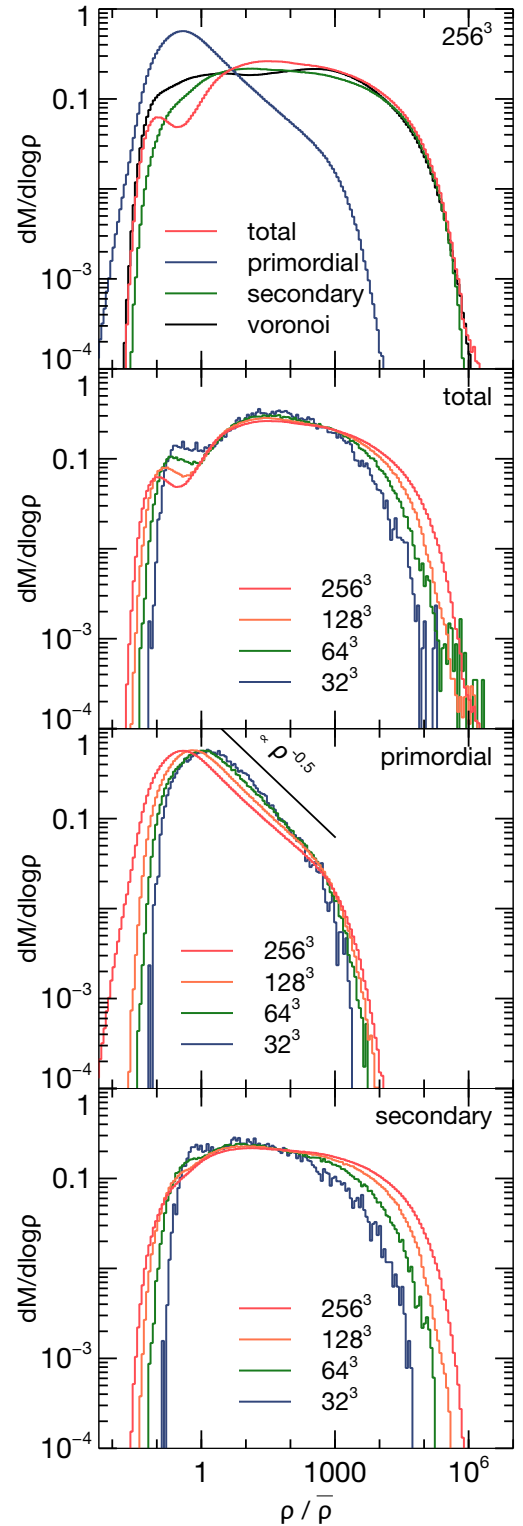


**Figure 11.** Mass-weighted density distributions. The top left panel shows the histogram for four different densities defined at the particle locations for the  $256^3$  run. The density estimated from Voronoi tessellation, the total sheet dark matter density, the primordial stream density and the secondary stream density. The results of the resolution study is given in the other three panels. The total space density is given in the top right panel. The bottom left is the mass-weighted density pdf of sheet density in the primordial stream. The bottom right panel gives the density contributed by material that is not in the primordial stream.

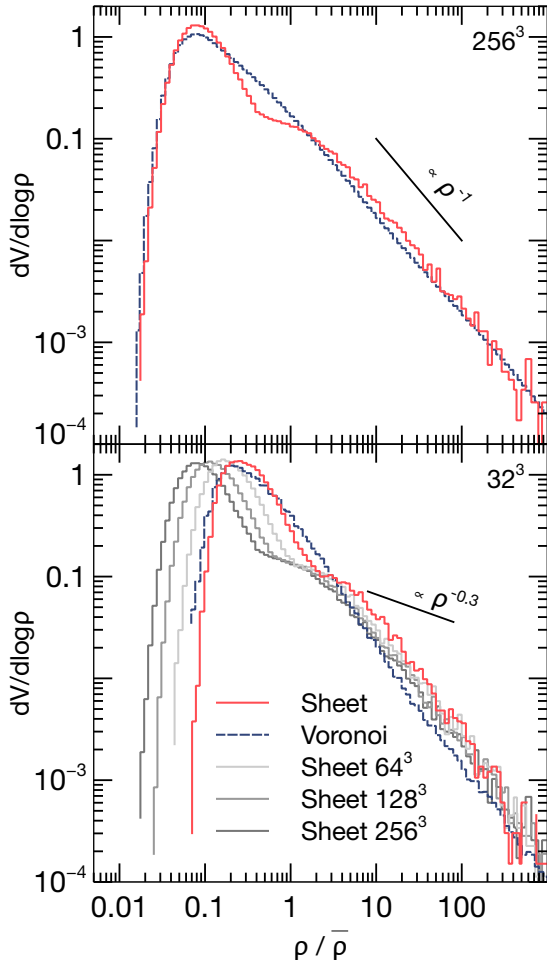


**Figure 12.** Volume-weighted density distributions. The top panel shows the histograms for the  $256^3$  run, the lower those for the  $32^3$  run. The density estimated from Voronoi tessellation is shown with a dashed line, the total sheet dark matter density with a solid line. At both resolutions, both the Voronoi and the stream density approach a  $\rho^{-1}$  power-law at high densities, also the two methods produce different estimates at intermediate densities of  $\rho/\bar{\rho} \sim 10$ .

while the total mass weighted density distribution is at much higher densities. The reason is that all the streams not inside the primordial stream contributing to the density at the location of the particle contribute much more to the total density at high densities. That distribution is given by the green line in the top panel labelled as “secondary”. There is an apparent power law part in the primordial stream densities visible. We will discuss this further when considering volume weighted distributions. These are given in Figure 12 where we show the volume weighted dark matter density. The total densities we estimate with our method are labelled as “Sheet”. We also indicate the resolution of the dark matter simulation used to compute it. The median of the stream density is 1.2 but its average is 26 times the mean. We also do not expect these numbers to converge as one continues to increase the resolution.

Let us discuss one interesting “rule of thumb” to describe some of the density distributions first. It is illustrated in Figure 13 where we plot the total space density in units of the primordial stream density measured at particles, divided by the number of streams at that location. Despite the enormous

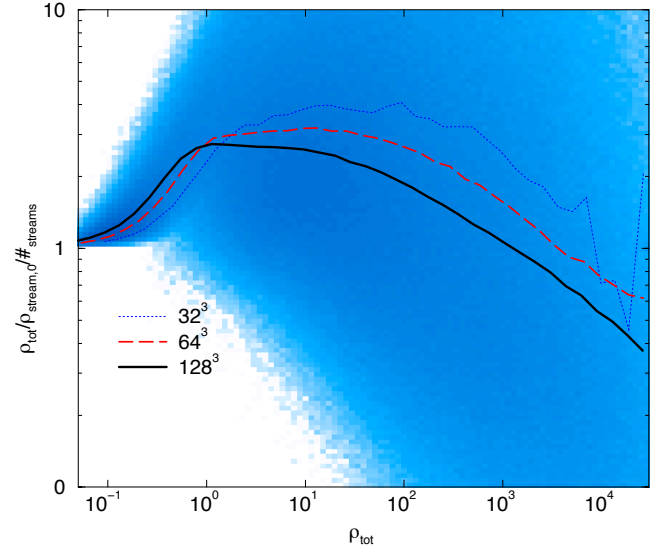


**Figure 13.** A rough rule of thumb. There is a large scatter between the primordial stream density and the total density at the particles as shown for the  $128^3$  data in the background. However, on average a good estimate of the total density is provided by the product of the number of streams times the density in the particles primordial stream. The exact values are not converged in the simulations. However, the estimate is good to a factor of three for the higher resolution calculations.

scatter between the primordial stream density and the total space density, as shown by the shaded region, the mean is good to within a factor of a few at all densities that our simulations probe. This result agrees with the results of Vogelsberger & White (2011) (their Fig. 7 and 8) although their approach tracks stream density explicitly in the simulations and they use dramatically higher resolution simulations allowing them to track many more streams.

We also compared our new density estimates with the corresponding results from another density estimator, which finds the unique Voronoi cells around each particle. The density in that volume is then simply defined as the mass of the enclosed particle divided by that volume element. Schaap & van de Weygaert (2000) and Pelupessy et al. (2003) have developed their DTFE density estimator which is more advanced and employs averaging over nearby tetrahedral cells. These authors give comparisons of that estimator to the smooth kernel estimates to the otherwise popular by Smoothed-Particle Hydrodynamics estimator. DTFE as well as the simple Voronoi estimator we use tessellates the entire volume and has no parameters and as such is a well suited benchmark for comparison.

Quite strikingly, at low and high densities our density estimate is very similar to the Voronoi volume based density estimators (Figure 14). Both methods do not converge at the very low density tail. This is physical in that the simulations model smaller voids when the resolution is increased. These can achieve lower densities than their larger counterparts in lower resolution simulations. So, at higher resolutions, it is not surprising to see a tail grow at those lowest densities. Also, the peak distribution shifts continuously to lower densities as more particles are employed. Significant differences in the volume fraction at a given density of our method with the Voronoi method are seen at intermediate densities around the mean density. This is understandable as the volumes that the

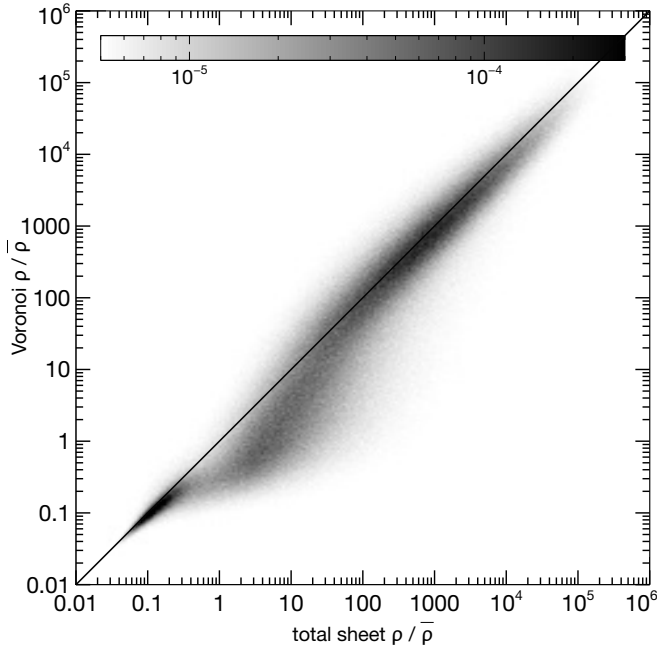


**Figure 14.** Two dimensional histogram comparing the Voronoi density estimate vs. the total sheet density. The correspondence is quite good. The largest difference is observed for values between a third and thirty times the mean density of dark matter. The Voronoi density estimators overestimates the volumes in regions around filaments and sheets.

Voronoi tessellation provides, tend to connect particles in the voids to the particles in the sheets and filaments. At that point it spreads particles in filaments into volumes that are larger and estimates consequently lower densities. In fact, these estimates are very significantly different. So much so that if we integrate the density from our method over the volumes computed from the Voronoi estimator the total mass in the box is overestimated by more than a factor of ten.

### 3.5 Radial profiles of haloes

Navarro et al. (1996) have discovered a universal radial profile of the dark matter density in virialized haloes. This is one of the key findings of cosmological N-body simulations and a large body of literature has largely confirmed the finding. We will give these profiles next. To get the best possible estimate, we choose 100,000 test positions and bin these in 50 radii, spaced logarithmically in radius. Figure 15 summarizes our findings. The densities computed from the dark matter sheet are somewhat shallower and have about 50% larger central densities at all resolutions for the single halo we have analyzed. Physically, it is conceivable that volume elements formed by particles on radial orbits oscillate such that the bounding regions have a higher probability to be found at large radii while still contributing to the density interior at small radii. Similarly, one can picture particles of the sheet orbiting the center at larger radii such that the volume element they span can contribute to the center. Our method has a well defined density at all radii and it is bound to be a constant at the lowest of radii where one averages always over the same tetrahedra. At large radii, the new density estimate and the Voronoi estimates all agree extraordinarily well. This is true even in the infall region. The Voronoi estimates at all radii are perfectly

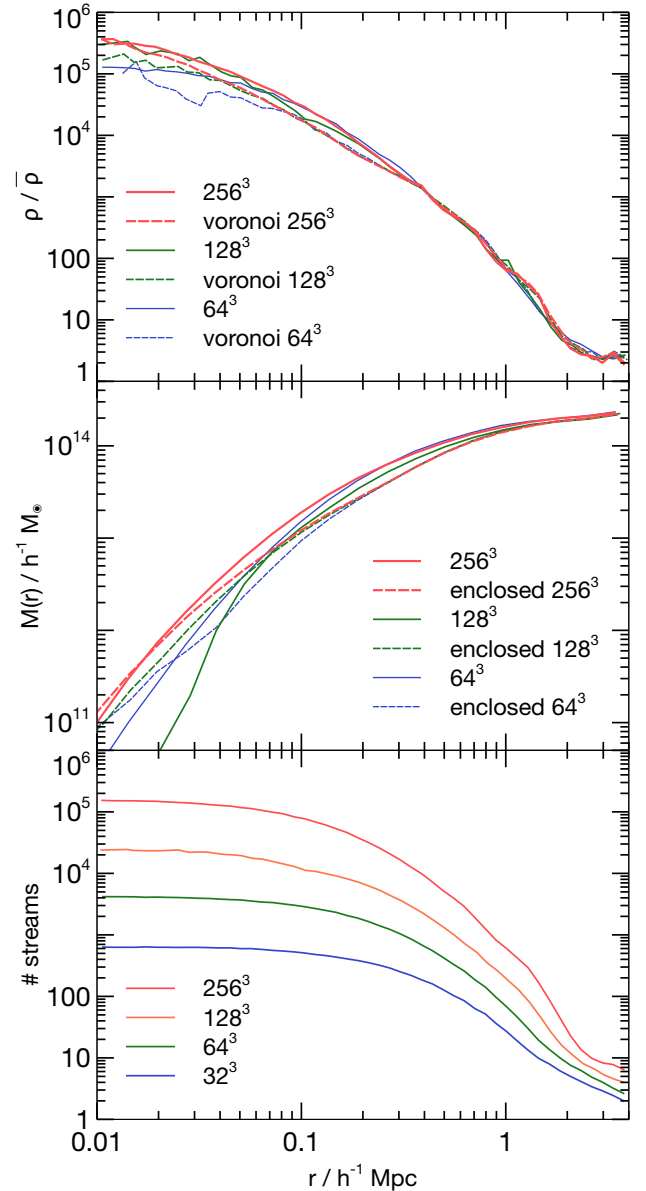


**Figure 15.** Dark Matter density profile in the most massive halo of  $2 \times 10^{14} M_{\odot}$  at redshift zero.

consistent with a simpler estimate based on the particle mass binned in shells divided by the shell volume (not shown).

The masses included within a radius do converge also quite well with our estimate being consistently slightly higher at a given radius. This is understandable as mass from particles outside a given radius can contribute if they span a volume element that has nodes inside the radius.

The number of streams that contribute to the profile are given in the lower panel of Figure 15. Not surprisingly, these increase with increasing resolution. If one scales them by factors of eight between increasing resolutions, some closer convergence is observed. Between the  $128^3$  and  $256^3$  simulations, there remains a difference of about 30% which is likely just due to streams contributing from larger radii to the regions inside the particles spanning the volume element.

It certainly would be interesting that the dark matter density profile in the central parts of haloes could be different than one measures from measuring dark matter particles in-

side a given radius. It is also suggestive how well our density profiles converge from  $128^3$  to  $256^3$  particles. However, if the mass profile were indeed different, also the forces contributing to the particle motions would be changed. So even if our density estimator were more accurate, one could not prove that the result shown in Figure 15 is the correct physical one until one has evolved the dark matter sheet consistently, i.e. using accelerations created by the density distribution of the actual sheet elements. We discuss some potential approaches to carry out such simulations in the discussion section.

### 3.6 Velocity dispersions and the dark matter “entropy”

While our method gives access to the full fine grained phase-space structure, we chose to only show moments to serve as an example of what the method is good for, and to be able to compare to work done on this previously. While the collisionless fluid does not experience microphysical collisions, the scattering provided by the time-varying gravitational potential leads to mixing in phase-space. The velocity dispersion of the particles is a measure of the effective pressure of the dark matter, which is of relevance for understanding the dynamical structure of orbits, i.e. e.g. the expectations of how observable stars move in the DM potential. Figure 16 summarizes the radial profiles of the velocity dispersion for the same halo we have analyzed above for density profiles. We again draw particles on random position over spherical shells for which measure the stream-density-weighted bulk velocity, subtract it from the stream-density-weighted local velocity dispersion, which we then average to get the velocity dispersion in radial shells.

These velocity dispersions differ quite significantly from the similarly termed quantities presented previously (e.g. Navarro et al. 2010, and references therein). While this may seem surprising, one has to keep in mind that we measure the dispersion at a single point, i.e. we do not carry out any averaging over volume. Dispersions quoted in the past measured a combination of a bulk and local dispersion. This will not only have large sampling error but also confuse turbulent bulk motions with actual microphysical velocity distributions. Indeed, we can see that our measured velocity dispersion does not converge at scales of about one half the virial radius, as only about one thousand streams contribute there for our highest resolution results. The distribution functions at this location will be quite anisotropic and a single temperature will be a bad fit (see below). The halo is remarkably cold in the center – having less than half the velocity dispersion expected from the virial velocity. In the same figure, we also show the pseudo phase-space density of Taylor & Navarro (2001) which has been found to be a perfect power law entirely independent of resolution (Navarro et al. 2010). When we measure the average of only the fine grained quantities, as shown in Figure 16, this perfect powerlaw disappears. This suggests that much of the measure is dominated by large scale bulk flows. It is worthwhile to explore this further with higher resolution simulations, where one can more confidently separate thermal motions from the bulk velocity dispersion.

It is though just as interesting to check the actual distribution function of dark matter velocities at a given point. The seminal work of Lynden-Bell (1967) discussed this in the context of stellar systems. The global distribution has been measured from simulations many times (see e.g. Hoefft et al.

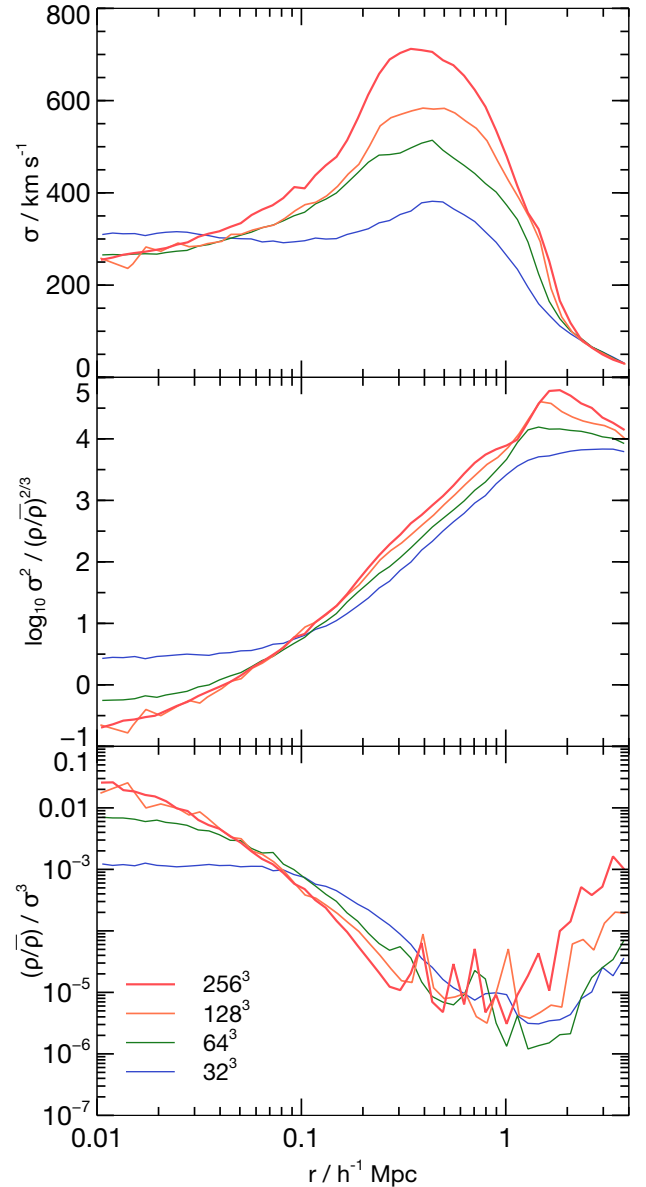


**Figure 16.** Radial spherically averaged profiles of the velocity dispersion (top), the dark matter “entropy”  $\sigma^2/(\rho/\bar{\rho})^{2/3}$  and the pseudo phase-space density for the same halo as in Figure 15. The velocity dispersion is remarkably flat inside about one tenth of the virial radius. The dark matter “entropy” profile also shows signs of already converging at the modest resolutions employed here.

2004; Wise & Abel 2007; Navarro et al. 2010; Vogelsberger et al. 2009) but to the best of our knowledge this was never done at individual points in the simulations. Figure 17 summarizes the distributions found at three different points in the most massive halo. We show it at the center where a relatively hot component overlays a colder one. At the center the distributions of the individual velocity components have peaks that almost coincide and widths which are quite similar as well. They are not too far from an isotropic Maxwell-Boltzmann distribution in their cores. As we step out in radius, the situation changes rapidly and the microphysical flow structure clearly shows more and more anisotropy. Interestingly, a quite hot component is seen along the  $x$  direction. At the same the velocity distribution in the  $y$  direction is the coldest at all radii.

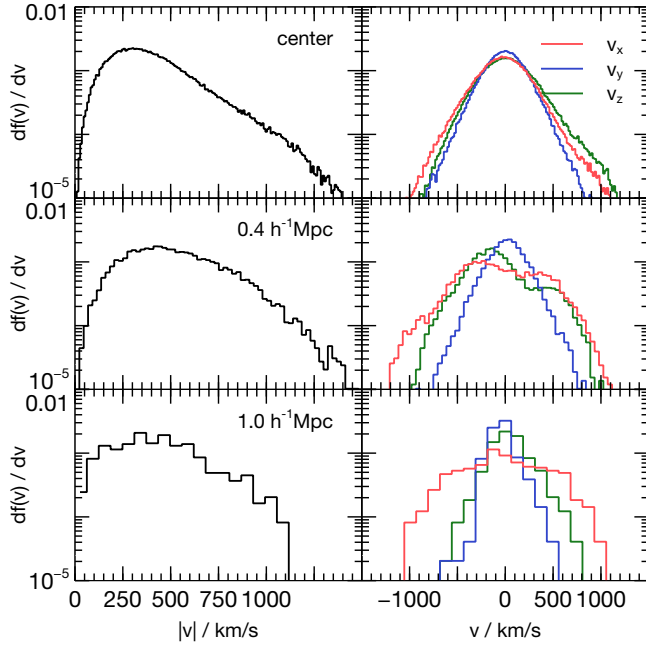


**Figure 17.** The velocity distribution function binned in velocity space at three points at varying distance from the center of the halo (left panels) and the individual distributions of the velocity components (right). We used 200, 80 and 30 bins for the points at the center,  $0.4 h^{-1}\text{Mpc}$  and  $1 h^{-1}\text{Mpc}$  from the center along one axis. These had 150,000, 13,000 and 400 individual streams that contributed.

These distributions are consistent with the visual impression obtained from the velocity dispersion slice in Figures 18 and 16 which also shows that some of the hottest DM fluid elements are found just inside the virial radius.

It is remarkable how much physics can be learned from even these low resolution simulations analyzed here. For the halo we just discussed, there are not even 600,000 dark matter particles inside the virial radius of  $1.4 h^{-1}\text{Mpc}$ . At the same time, there are already enough streams to compute meaningful measures of the structure of phase-space. We are certainly looking forward to carrying out a more detailed analysis on higher resolution simulations. This point is born out by the visual impression given by infinitesimal slices as shown in 18, which we will describe next.

### 3.7 Slices of Density and Dark Matter “Entropy”

To aid in the interpretation of the profiles, we have just presented, we also give two dimensional slices through the dark matter density and “entropy”, which we define analogously to the adiabats used when studying e.g. galaxy clusters hydrodynamically simply as  $S_{DM} = \sigma^2/(\rho/\bar{\rho})^{2/3}$ , which then just has units of the square of a velocity. Also the average number of streams contributing to every point on the slice is given. Material from the voids falls in perfectly cold. We can think of the velocity dispersion as a measure of the temperature of the fluid. It is ill defined in the single stream regions falling from the voids. However, these carry very little mass. Then we see a region that extends to about two Mpc from the center which hosts multi-stream material of the order of about ten streams. The virial radius which is approximately one Mpc shows a marked increase in the velocity dispersion and a much

smoother density structure. Even on this scale, we can see the cold central isothermal part of the object, both in the velocity dispersion and in the entropy. Substructure is easily seen as cold low entropy material embedded in the hot halo. Many of the structures seen here are very reminiscent of adiabatic hydrodynamics simulations of galaxy clusters Frenk et al. (1999) and even first star formation Abel et al. (2002) where gas enters haloes predominantly through filaments and shock heats, resulting in a halo with rising entropy profiles with radius.

### 3.8 General interpolation to any point in space

There are large advantages to have well defined grids which allows one to interpolate to any point in space. This is a very obvious observation of course, it is, however, a large step forward in understanding dark matter simulations. This has led to a number of approaches being devised that allow such interpolation, such as the methods discussed in the introduction. Here we discuss but a few approaches on how to use the tessellated dark matter sheet for interpolation.

When probing the sheet at the particle locations we find the primordial stream densities, total space densities, number of streams, velocities etc.. Hence we have sampled the full volume and have a non-uniform distribution of the fields we aim to interpolate. One may choose to achieve further interpolation by using a distance weighted estimate from the nearest particle locations. An efficient way to find two dimensional slices is to take all tetrahedron edges and compute their intersections with the plane to be interpolated to. Along every edge one can now linearly interpolate the values of the vertices to the plane. The resulting scattered data on the plane is then triangulated again and interpolated with linear interpolation between nodes. As an example the slice of the total sheet density is shown in Figure 19 which also gives a visual clue to how cloud in cell interpolation would sample the density field.

Similarly, this allows us to extract one dimensional skewers at arbitrary resolution from N-body simulations. As an example, Figure 20 compares the velocity along a random line through the volume for different resolutions. The large scale modes are all consistent by design. It is interesting to see that convergence is quite slow and suggests to extend this analysis rigorously to much higher resolutions.

## 4 DISCUSSION

Vogelsberger et al. (2008); White & Vogelsberger (2009); Vogelsberger & White (2011) develop the GDE formalism to allow the calculation of the primordial stream density. Their approach modifies the simulation code to integrate an evolution equation of the tidal tensor along with every particle trajectory. In principle, this can be much more accurate since the local stretching of the dark matter sheet is calculated at every time step of the calculation. It will be of great interest to compare our approach to theirs in detail. This will require to carry out the calculations with both methods on an identical simulation to facilitate a particle by particle comparison. This should be particularly interesting given that our method can next to the primordial stream density also provide the total space density and number of streams at every location. Since our approach also gives full fine grained phase-space information, it seems plausible one could combine both approaches which inherits the advantageous of both.



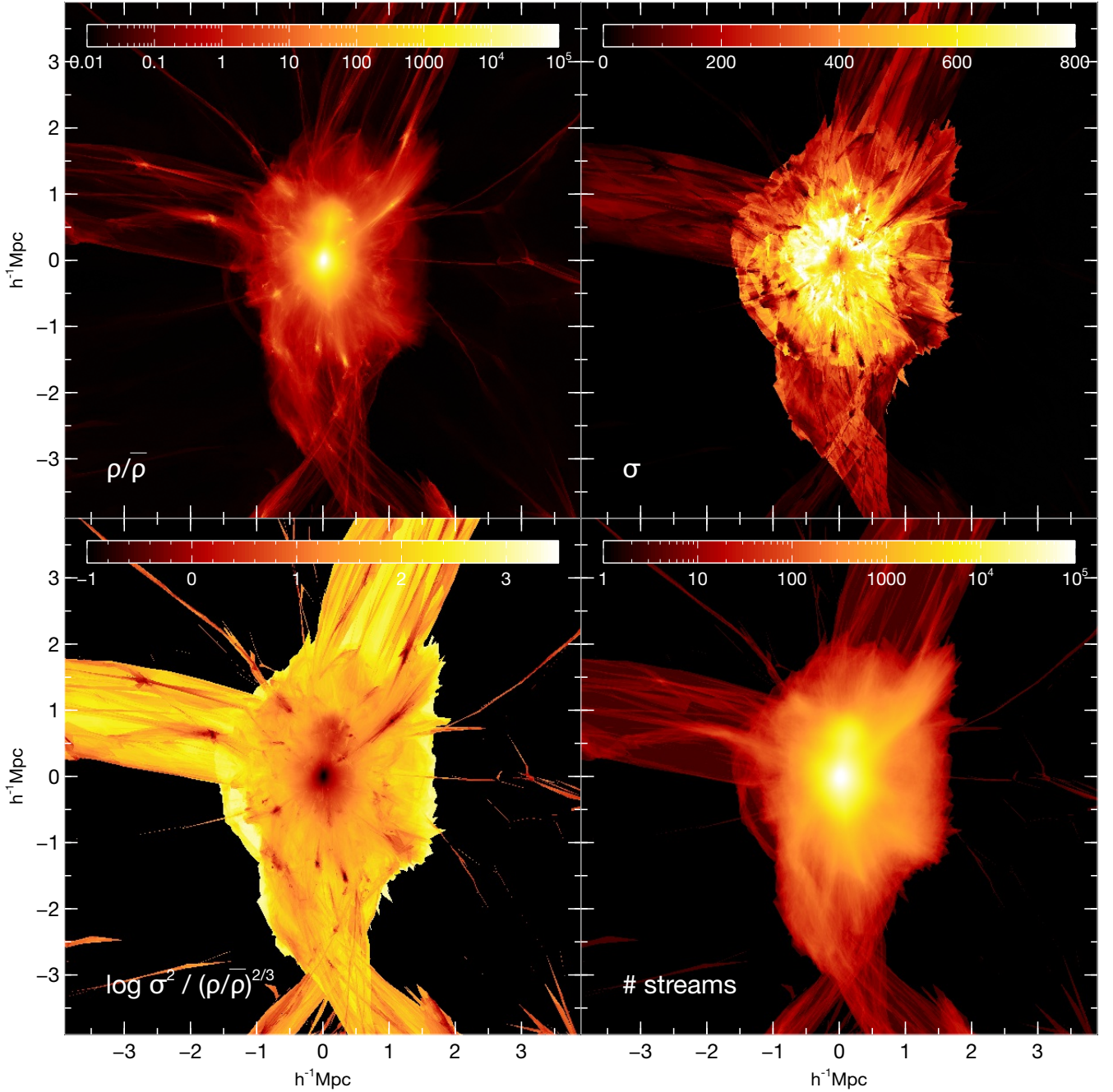


**Figure 18.** Infinitesimally thin slice through the 256<sup>3</sup> simulations for the most massive halo. We show the density in units of the mean density (top left), the stream-density weighted velocity dispersion in kilometers per second (top right), the dark matter entropy [(km/s)<sup>2</sup>] computed from the density and stream weighted velocity dispersion  $\sigma^2/(\rho/\bar{\rho})^{2/3}$  and the average number of streams (not stream density weighted) at the bottom right. Clearly our approach gives information so far thought inaccessible from current simulations.

More generally, both the GDE and our approach suggest a number of possible approaches to improve the accuracy of N-body calculations. Almost all current cosmological N-body solvers employ the particle mesh method at least for the largest scales in the calculation. The cloud in cell approximation is used to interpolate the dark matter particles to a grid on which the gravitational potential will be evaluated before differencing it to obtain the gravitational forces on the particles. Since one integrates twice to get the potential from the density field and only differentiates once this method gives reasonably smooth gravitational forces. However, it inherently

models a very noisy inaccurate density distribution obtained from CIC which will have the largest relative errors in poorly sampled regions such as voids, pancakes and filaments (see Figure 19).

We have shown that our density estimator would have significantly more fidelity and reliability for these large regions. It is in principle quite straightforward to modify an existing particle mesh code to make use of our density estimator and then derive more accurate potentials and forces from it. It only involves the interpolation step to the grid. Interpolating the contribution back to the particle positions one could make

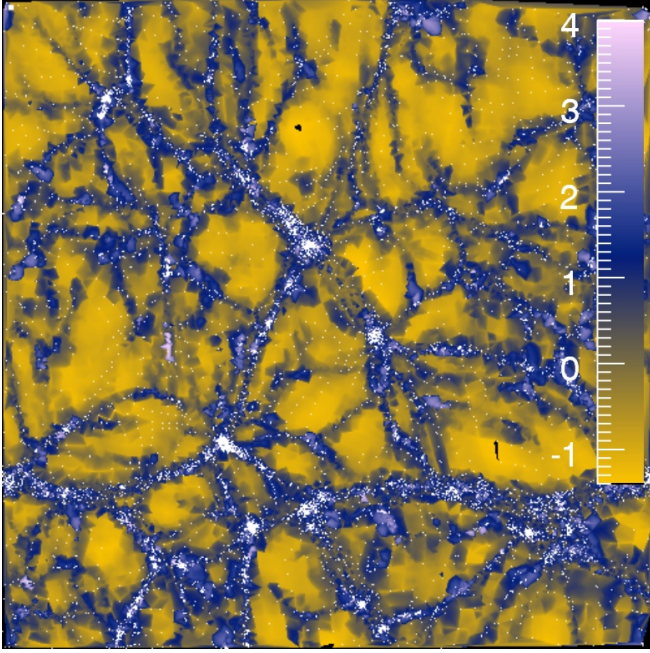


**Figure 19.** The logarithm of the density in an infinitesimally thin slice in units of the mean density for the  $128^3$  simulation. The white dots show the location of the particles which would contribute to a cloud in cell interpolation on a grid with cells as large as the mean particle spacing. The squares at the top left show the area to which these individual particles would contribute to at their locations.

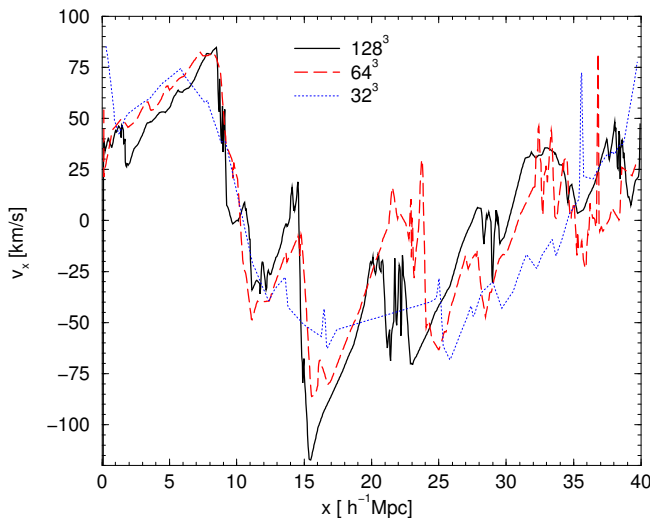


**Figure 20.** The velocity field along a one dimensional line extracted using tetrahedron edges to interpolate to a slice plane. The differences in resolution are understandably quite large given the large range of mass resolution of the simulations. The large scale features remain recognizable even at the lowest of resolutions. The “N-shaped” infall regions are seen for many structures.

use of the known analytical solutions to the Newtonian potential of homogeneous polyhedra (Waldvogel 1979). Similarly, these analytic formulae could be applied in direct summation and tree-based codes. A priori it may seem difficult to imagine how to construct trees efficiently when considering that the tetrahedra may become exceedingly distorted and elongated and would cover many nodes of the tree. However, any

new code would most likely ever only be employed using local mesh refinement given that the tessellation we suggest gives many opportunities to discover the regions of the flow which may be prone to large errors. The local curvature of the flow compared to the tetrahedra edges is one measure but also the axis ratio of individual tetrahedra provides an estimate where the flow would benefit from refinement. The key of any such new method will have to be to fully consider the dark matter as a fluid so that spurious particle-particle interactions may be avoided and multi-mass resolution becomes feasible. Given a locally refined mesh, tree structures will remain useful in rapidly finding neighbours and retain  $n \log n$  scaling.

There are a number of improvements possible that will help to develop our GPU assisted volume rendering further. Using vertex values and some form of Shepard’s method to carry out distance dependent weighting should still likely be very fast on current GPUs even when drawing billions of tetrahedra.

Higher order interpolation in fact could be another avenue to improve on the method suggested here. We have only implemented the very simplest of ideas. Namely that volume elements in phase-space are uniformly filled with the dark matter fluid. This is similar in spirit to donor cell methods used decades ago for hydrodynamical flows. We believe that it will be possible to improve on our approach significantly. Up-winded schemes with linear reconstruction were a large gain in accuracy in numerical fluid dynamics and similar improvements are certainly possible here.

Given that one now has a natural grid that can be used to interpolate any state variables as well as the full fine-grained phase-space structure, one can also define differentials on it. Consequently, it becomes possible to study vorticity, divergences as well as carry out the Cauchy-Stokes decomposition of the dark matter velocity fields. This way one can separate bulk, shear and rotational components of the velocity fields which undoubtedly will make it possible to track down the physical origin of dark matter density profiles as well as to better understand the internal structure of haloes and the cosmic web.

There is a remarkably large number of applications where we think our method can aid to gain new insights. Whether it is gravitational lensing to find more accurate lensing potentials to studying the origin of the angular momentum profiles (see e.g. Fig. (12) in Bullock et al. 2001). Obviously the connection between dark matter and the baryons they host can be explored much more fully now as well.

As we were preparing this manuscript, Shandarin et al. (2011) posted a paper on the electronic preprint server which explores the same basic idea as the one we present here. The concept of tessellating phase-space and tracking the dark matter sheet is identical to ours. Details of the implementation and what to think of as fundamental parts of the approach are not the same. Their choice of tessellation is quite different. In their approach the tetrahedra are thought of as the fundamental resolution elements and no averaging is done over adjacent tetrahedra. This is in principle problematic since as we argued we cannot assume that the dark matter fluid is indeed confined exactly to the tetrahedron shapes as these are generated on smaller length scales than the resolution of the underlying N-body simulation. Also their choice of tetrahedra is different. They pick the minimal combination of tetrahedra of the unit cube possible which has five elements where one of them is twice the volume as the other four and itself does not tesse-

late the space uniformly. Consequently they alternately rotate adjacent cubes such that the edges of tetrahedra never cross. This is effective albeit likely more cumbersome for a practical implementation. The powerlaw Shandarin et al. (2011) gives for the volume fraction as a function of the number of streams ( $f_V(N_{stream}) = 0.93 N_{stream}^{-2.82 \pm 0.05}$ ) is to be compared with our Figure 7. Their power law fits approximately our  $32^3$  run and likely just reflects the fact that the single simulation they study had approximately two times worse mass resolution than our  $32^3$  run with an effective gravitational softening length about five times larger than ours. So both approaches do agree. We at this time would not attach a special meaning to this powerlaw as it clearly is strongly resolution dependent with our highest resolution run giving something close to  $N_{stream}^{-2}$ .

## 5 SUMMARY

We presented an approach to better understand the dynamics of cold collisionless fluids. We apply it by post-processing N-body simulations and document the significant improvement it represents over any previous attempts to quantify the macroscopic and microscopic parts of the dark matter fluid flow. In particular, we show new results for density estimates, a dark matter “entropy”, bulk velocities, velocity distribution functions – many of which are computed here for the first time. We are confident that our approach to tracing the dark matter sheet in phase-space gives important physical insights which were inaccessible with previous approaches.

## ACKNOWLEDGEMENTS

T.A. is grateful for numerous conversations with Greg Bryan in the past ten years on how one might solve for dark matter dynamics directly in phase-space and acknowledges support by the National Science foundation through award number AST-0808398 and the LDRD program at the SLAC National accelerator laboratory as well as the Terman fellowship at Stanford University. He also acknowledges help by Patrick Abel in constructing tetrahedra from paper which helped considerably in understanding the many possible options of tessellations of the dark matter sheet.

## REFERENCES

- Abel T., Bryan G. L., Norman M. L., 2002, *Science*, 295, 93  
 Afshordi N., Mohayaee R., Bertschinger E., 2009, *Phys. Rev. D*, 79, 083526  
 Alard C., Colombi S., 2005, *MNRAS*, 359, 123  
 Aragón-Calvo M. A., Jones B. J. T., van de Weygaert R., van der Hulst J. M., 2007, *A&A*, 474, 315  
 Aragón-Calvo M. A., Platen E., van de Weygaert R., Szalay A. S., 2010, *ApJ*, 723, 364  
 Arnold V. I., Shandarin S. F., Zeldovich I. B., 1982, *Geophysical and Astrophysical Fluid Dynamics*, 20, 111  
 Ascasibar Y., 2010, *Computer Physics Communications*, 181, 1438  
 Bernardeau F., van de Weygaert R., 1996, *MNRAS*, 279, 693  
 Bertschinger E., 1998, *ARA&A*, 36, 599  
 Binney J., 2004, *MNRAS*, 350, 939  
 Bryan G. L., Norman M. L., 1997, in Clarke D. A., West M. J., eds, *Computational Astrophysics; 12th Kingston Meeting on Theoretical Astrophysics Vol. 123 of Astronomical Society of the Pacific Conference Series, Simulating X-Ray Clusters with Adaptive Mesh Refinement*. pp 363+  
 Buchert T., Bartelmann M., 1991, *A&A*, 251, 389  
 Bullock J. S., Dekel A., Kolatt T. S., Kravtsov A. V., Klypin A. A., Porciani C., Primack J. R., 2001, *ApJ*, 555, 240  
 Colberg J. M., Pearce F., Foster e. a., 2008, *MNRAS*, 387, 933  
 Couchman H. M. P., 1991, *ApJ*, 368, L23  
 Cuperman S., Harten A., Lecar M., 1971, *Ap&SS*, 13, 411  
 Diemand J., Kuhlen M., Madau P., Zemp M., Moore B., Potter D., Stadel J., 2008, *Nature*, 454, 735  
 Efsthathiou G., Davis M., White S. D. M., Frenk C. S., 1985, *ApJS*, 57, 241  
 Frenk C. S., White S. D. M., Bode P., Bond J. R., Bryan G. L., Cen R., Couchman H. M. P., Evrard A. E., Gnedin N., Jenkins A., Khokhlov A. M., Klypin A., Navarro J. F., Norman M. L., Ostriker J. P., Owen J. M., Pearce F. R., Pen U., Steinmetz M., Thomas P. A. e. a., 1999, *ApJ*, 525, 554  
 Gibbs J., 1902, *Elementary principles in statistical mechanics, developed with especial reference to the rational foundation of thermodynamics*. Library of American civilization, Scribner’s sons  
 Hahn O., Abel T., 2011, *MNRAS*, 415, 2101  
 Hahn O., Porciani C., Carollo C. M., Dekel A., 2007, *MNRAS*, 375, 489  
 Hoeft M., Mücke J. P., Gottlöber S., 2004, *ApJ*, 602, 162  
 Hogan C. J., 2001, *Phys. Rev. D*, 64, 063515  
 Lynden-Bell D., 1967, *MNRAS*, 136, 101  
 Maciejewski M., Colombi S., Alard C., Bouchet F., Pichon C., 2009, *MNRAS*, 393, 703  
 Navarro J. F., Frenk C. S., White S. D. M., 1996, *ApJ*, 462, 563  
 Navarro J. F., Ludlow A., Springel V., Wang J., Vogelsberger M., White S. D. M., Jenkins A., Frenk C. S., Helmi A., 2010, *MNRAS*, 402, 21  
 Neyrinck M. C., 2008, *MNRAS*, 386, 2101  
 Peebles P. J. E., 1971, *A&A*, 11, 377  
 Peluussy F. I., Schaap W. E., van de Weygaert R., 2003, *A&A*, 403, 389  
 Rasio F. A., Shapiro S. L., Teukolsky S. A., 1989, *ApJ*, 344, 146  
 Schaap W. E., van de Weygaert R., 2000, *A&A*, 363, L29  
 Shandarin S., Habib S., Heitmann K., 2011, *ArXiv e-prints*  
 Shandarin S. F., Zeldovich Y. B., 1989, *Reviews of Modern Physics*, 61, 185  
 Sharma S., Steinmetz M., 2006, *MNRAS*, 373, 1293  
 Shen J., Abel T., Mo H. J., Sheth R. K., 2006, *ApJ*, 645, 783  
 Springel V., 2005, *MNRAS*, 364, 1105  
 Springel V., White S. D. M., Frenk C. S., Navarro J. F., Jenkins A., Vogelsberger M., Wang J., Ludlow A., Helmi A., 2008, *Nature*, 456, 73  
 Springel V., White S. D. M., Jenkins A., Frenk C. S., Yoshida N., Gao L., Navarro J., Thacker R., Croton D., Helly J., Peacock J. A., Cole S., Thomas P., Couchman H., Evrard A., Colberg J., Pearce F., 2005, *Nature*, 435, 629  
 Springel V., Yoshida N., White S. D. M., 2001, *New Astronomy*, 6, 79  
 Stadel J. G., 2001, PhD thesis, UNIVERSITY OF WASHINGTON

- Stiff D., Widrow L. M., Frieman J., 2001, *Phys. Rev. D*, 64, 083516
- Taylor J. E., Navarro J. F., 2001, *ApJ*, 563, 483
- Teyssier R., 2002, *A&A*, 385, 337
- Tremaine S., 1999, *MNRAS*, 307, 877
- Vera-Ciro C. A., Sales L. V., Helmi A., Frenk C. S., Navarro J. F., Springel V., Vogelsberger M., White S. D. M., 2011, *MNRAS*, 416, 1377
- Vogelsberger M., Helmi A., Springel V., White S. D. M., Wang J., Frenk C. S., Jenkins A., Ludlow A., Navarro J. F., 2009, *MNRAS*, 395, 797
- Vogelsberger M., White S. D. M., 2011, *MNRAS*, 413, 1419
- Vogelsberger M., White S. D. M., Helmi A., Springel V., 2008, *MNRAS*, 385, 236
- Wadsley J. W., Stadel J., Quinn T., 2004, *New Astronomy*, 9, 137
- Waldvogel J., 1979, *Zeitschrift Angewandte Mathematik und Physik*, 30, 388
- White S. D. M., Vogelsberger M., 2009, *MNRAS*, 392, 281
- Wise J. H., Abel T., 2007, *ApJ*, 665, 899
- Zel'Dovich Y. B., 1970, *A&A*, 5, 84